



RESEARCH LETTER

10.1002/2014GL059968

Key Points:

- The earthquake involves primarily a single subhorizontal fault plane
- Both phase transformation and thermal instability contributed to the earthquake
- Thermal variation of the slab explains the frequency-dependent seismic radiation

Supporting Information:

- Readme
- Figures S1–S11 and Table S1

Correspondence to:

L. Meng,
meng@ess.ucla.edu

Citation:

Meng, L., J.-P. Ampuero, and R. Bürgmann (2014), The 2013 Okhotsk deep-focus earthquake: Rupture beyond the metastable olivine wedge and thermally controlled rise time near the edge of a slab, *Geophys. Res. Lett.*, 41, 3779–3785, doi:10.1002/2014GL059968.

Received 21 MAR 2014

Accepted 14 MAY 2014

Accepted article online 16 MAY 2014

Published online 2 JUN 2014

The 2013 Okhotsk deep-focus earthquake: Rupture beyond the metastable olivine wedge and thermally controlled rise time near the edge of a slab

Lingsen Meng¹, Jean-Paul Ampuero², and Roland Bürgmann³

¹Earth, Planetary and Space Sciences, University of California, Los Angeles, California, USA, ²Seismological Laboratory, Division of Geological and Planetary Sciences, California Institute of Technology, Pasadena, California, USA, ³Berkeley Seismological Laboratory and Department of Earth and Planetary Science, University of California, Berkeley, California, USA

Abstract The 2013 *M*8.3 Okhotsk earthquake involves two primary mechanisms of deep-focus earthquake rupture, mineral phase transformation of olivine to spinel and thermal shear instability. Backprojection imaging of broadband seismograms recorded by the North American and European networks indicates bilateral rupture toward NE and SSE. The rupture paths of the NE segment and other regional *M*7 earthquakes are confined in narrow regions along the slab contours, consistent with the phase transformation mechanism. However, the SSE rupture propagates a long distance across the slab and aftershocks are distributed across a ~60 km wide zone, beyond the plausible thickness of the metastable olivine wedge, favoring thermal shear weakening. While the NE rupture is only visible at high frequencies, the SSE rupture is consistently observed across a broad-frequency range. This frequency-dependent rupture mode can be explained by lateral variations of rise time controlled by thermal thinning of the slab near its northern end.

1. Introduction

A remarkable 610 km deep earthquake occurred on 24 May 2013, beneath the Sea of Okhotsk, west of the Kamchatka peninsula. The *M*8.3 (U.S. Geological Survey *W* phase solution) quake surpassed in magnitude the *M*8.2 1994 Bolivia earthquake, rendering it the largest deep-focus earthquake (focal depth > 300 km) ever recorded by modern seismology. The earthquake occurred near the NW corner of the seismogenic portion of the subducting Pacific slab, which is underthrusting the Okhotsk plate along the Kurile-Kamchatka subduction zone. The physical mechanism that triggers and sustains earthquake ruptures at this depth remains controversial [Frolich, 1989; Green and Houston, 1995]. Discrimination between the two main proposed mechanisms, phase transformation of olivine to spinel (confined within a metastable olivine wedge) and thermal shear instability, has eluded previous seismological observations [Chen, 1995; Silver and Beck, 1995; Kanamori et al., 1998; Tibi et al., 1999]. Most seismological studies of the Bolivia earthquake have favored rupture on a subhorizontal plane [Kikuchi and Kanamori, 1994; Goes and Ritsema, 1995; Antolik et al., 1996] and inferred a large rupture size beyond the metastable phase transformation zone [Silver and Beck, 1995; Antolik et al., 1996] unless slab thickening is invoked [Kirby et al., 1996]. An alternative rupture model that fits within a thin metastable olivine wedge involves an echelon rupture spanning multiple subhorizontal fault planes at different depths. However, these two rupture geometries cannot be distinguished by low-frequency source studies [Chen, 1995]. The Okhotsk event offers an exceptional opportunity to investigate the contribution of the two proposed physical mechanisms of deep-focus earthquakes and their connections to the thermal state of the subducting slab.

2. High-Resolution Backprojection of the Deep-Focus Earthquake

Taking advantage of the recently developed large regional seismic arrays and of the integration of seismic data across Europe, we are able to image the rupture process by backprojecting the teleseismic broadband seismograms (16 s to 4 Hz) recorded by the North American (NA) and European (EU) networks (Figure S1 in the supporting information). Backprojection (BP) aims at imaging the spatiotemporal distribution of seismic energy release of an earthquake rupture. We applied the Multitaper-MUSIC array processing technique [Meng et al., 2011] with the “reference window” strategy [Meng et al., 2013], which enables higher-resolution and weaker “swimming” artifacts than with standard beamforming methods. The relative simplicity and high

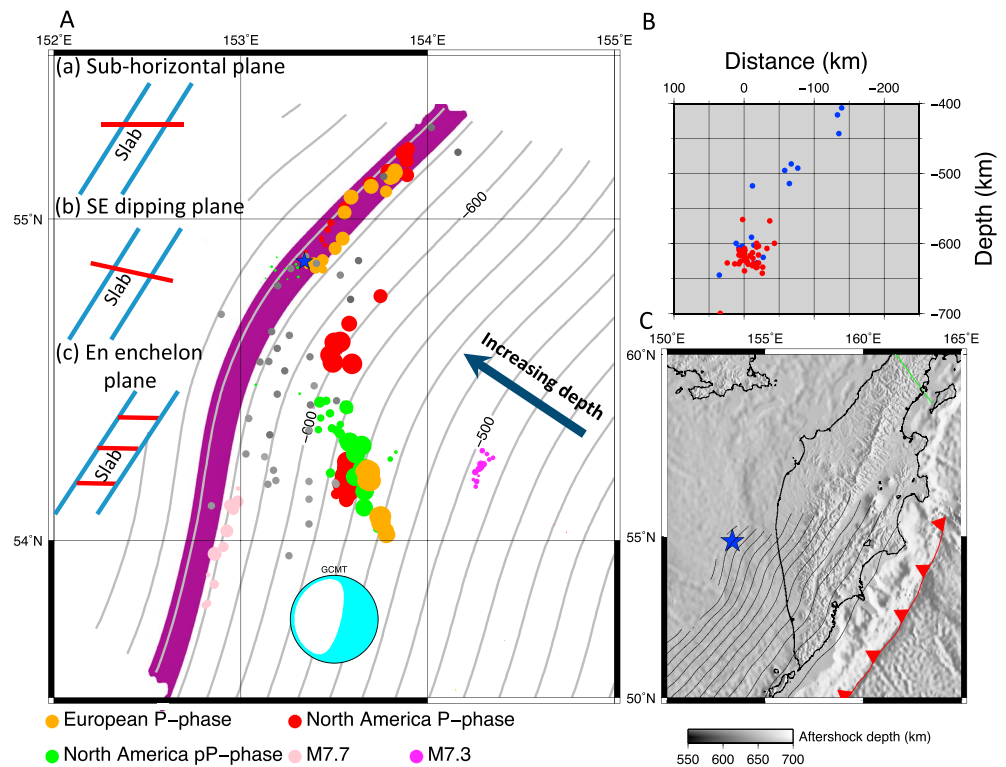


Figure 1. Comparison of BP results on a single subhorizontal plane. (A) The blue star indicates the main shock hypocenter. The GCMT moment tensor is shown as the cyan beach ball. The gray contours denote the Slab 1.0 model [Hayes *et al.*, 2012]. The purple band represents a ~15 km wide metastable olivine wedge centered on the hypocenter. The gray dots are the aftershocks in the International Seismological Centre catalog with horizontal location uncertainty smaller than 30 km. The top left sketch shows three candidate fault hypotheses: (a) a single subhorizontal plane extending beyond the metastable olivine wedge, (b) a plane dipping 18° SE extending beyond the wedge, and (c) en echelon faults with multiple subhorizontal planes confined within the slab. Colored circles indicate the locations of high-frequency radiation obtained by BP on a subhorizontal plane based on the P phase (0.5–2 Hz) (red) and pP phase (0.25–1 Hz) (green) recorded by the NA array and the P phase (0.5–2 Hz) recorded by the EU array (orange). The pP phase BP, done at a lower frequency than the direct P phase due to its lower coherency, misses the NE rupture due to the contamination by the P coda. Nevertheless, the three BP images on the subhorizontal plane (red, green, and orange) are in general consistent. The pink and magenta circles are results from the BP of the P phase recorded by the NA array for the 5 July 2008 M7.7 earthquake (depth: 646 km) and the 24 November 2008 M7.3 earthquake (depth: 505 km) respectively. (B) Historical seismicity (blue) and aftershocks (red) on a 200 km wide, along-dip cross-section profile across the source region (zero distance at the hypocenter). (C) The slab geometry and tectonic setting of the Kamchatka subduction zone.

coherency of the wavefield produced by very deep sources enables source imaging at higher frequencies than previously achieved in BP studies of shallow megathrust earthquakes [Ishii *et al.*, 2005; Meng *et al.*, 2011; Koper *et al.*, 2012].

2.1. Discrimination of the Candidate Fault Planes

The focal mechanism of the Okhotsk event (Global Centroid Moment Tensor Solution, Figure 1) is typical for deep earthquakes and consistent with downdip compression in a slab dipping about 50°W [Gorbatov and Kostoglodov, 1997]. The possible single-plane geometry of the fault is either subhorizontal or subvertical. The latter is often ruled out in intermediate to deep-focus earthquakes by a lack of vertical *P* wave directivity [Warren *et al.*, 2008]. Recent advances in backprojection (BP) source imaging also allow us to constrain the fault plane of the Okhotsk earthquake more conclusively than in previous studies [Ye *et al.*, 2013; Zhan *et al.*, 2014]. Fine depth variations of the rupture process and thus the fault geometry of deep earthquakes may be obtained by joint BP of the direct phase *P* and the depth phase *pP* [Kiser *et al.*, 2011], but this remains challenging for large earthquakes due to the variation of radiation pattern, directivity effects, incidence-dependent bias and the along-raypath trade-off. The result of our joint backprojection of *P* and *pP* phases on a 3-D volume (i.e., without assuming a fault plane) shows that the southern rupture front has a component of

downward propagation, spanning a depth extent of 30 km suggestive of a plane dipping 18° in the SE direction (opposite to the slab dip direction) (Figure S7). However, large uncertainties in this joint 3-D BP remain due to a dominant contribution of the more coherent P phase introducing a trade-off along its raypath (Figure S9). We therefore consider four candidate rupture geometries: a single subhorizontal plane, a subvertical conjugate plane, an echelon rupture on multiple subhorizontal planes within the slab, and a plane dipping 18° in the SE direction (Figure 1, inset). The BP results on a single subvertical plane shows an excessively large vertical rupture dimension of 300 km (see supporting information; Figures S5 and S11), which is not favored by the depth range of the aftershocks (Figure 1). However, the aftershock distribution cannot reliably discriminate rupture on a single horizontal plane [Ye *et al.*, 2013] and an echelon rupture on multiple horizontal planes distributed within the slab. We can nevertheless compare the separate BPs of P and pP, on a horizontal plane (Figure 1a) a SE dipping plane (Figure 1b) and on a dipping plane along the slab interface (Figure 1c), as a proxy for multiple horizontal planes distributed within the slab (BP is not sensitive to the fine-scale geometry of the echelon faulting). The horizontal BP is in general consistent across different phases and different arrays (Figure 1). The southern rupture shown by the BPs on a SE dipping plane, based on P and pP phases of the NA array and P phase of the EU array, are inconsistent (Figure S2). The slab-parallel BP is not amenable for this consistency check because it has sufficient resolution only for the P phase of the NA array (see supporting information). However, aided by synthetic tests, we find that the source obtained by the slab-parallel BP of the P phase is inconsistent with the horizontal BP of the pP phase (see Figures S2 and S3 and Table S1 in the supporting information). We therefore conclude that only the single horizontal plane hypothesis is consistent with the observed source images obtained from both P and pP phases.

2.2. Rupture Beyond the Metastable Olivine Wedge

The BP source imaging shows that the event involved bilateral rupture on NE and SSE trending segments (Figure 1) and allows estimation of the rupture dimensions on each segment. Previous studies proposed that the bilateral rupture is confined within the cold core of the slab [Ye *et al.*, 2013] or more specifically within the metastable olivine wedge [Zhan *et al.*, 2014]. Here we find that the NE rupture follows the slab contours. Although the absolute depth of the Slab 1.0 model in the source region has a large uncertainty due to the sparse local seismicity on which it is based, the curvature of the slab model is interpolated under smoothing constraints and includes information from the shallower slab geometry which is well constrained by more abundant seismicity [Hayes *et al.*, 2012]. The remarkable alignment of the NE rupture with the strike of the local Slab 1.0 contours is unlikely to be fortuitous and supports a smooth depth dependence of slab curvature. Further support is provided by our results of BPs of the 2008 $M7.7$ and $M7.3$ earthquakes based on 0.5–2 Hz *P* waves recorded by the NA array, which also show a remarkable alignment of the rupture path with the Slab 1.0 contours (Figure 1 and Figure S6). These observations provide evidence that the NE rupture was confined within the metastable olivine wedge. In contrast, the SSE rupture obliquely crosses the slab with a horizontal rupture length larger than 90 km (projecting to 60 km in the direction normal to the slab). The aftershocks are primarily distributed between the hypocentral depth contour of the slab and the SSE branch imaged by BP, suggesting a wide rupture area south of the hypocenter. This large dimension requires rupture propagation beyond the plausible thickness of a metastable olivine wedge; about 15 km at the relevant pressure-temperature conditions [Marone and Liu, 1997] or a more general estimate of 5 to 15 km [Kirby *et al.*, 1996].

An alternative hypothesis, based on low-frequency observations only, favors the phase transformation mechanism by proposing that the SSE rupture is aligned with the slab contours, provided a large error in the current model of the slab geometry [Zhan *et al.*, 2014]. Considering the rupture paths of the $M7$ class earthquakes and the NE rupture of the $M8.3$ earthquake revealed by our high-frequency analysis are indicative of the local slab strike direction (Figure 1), this hypothesis requires two sharp bends or tears in the slab, near the hypocenter and at the southern end of the rupture. While such complex geometry is not impossible, especially near the edge of a slab [Levin *et al.*, 2002], a narrow rupture zone confined within the metastable olivine core of the slab is incompatible with the wide aftershock distribution south of the hypocenter (Figure 1) and the wide slip distribution in finite fault models [e.g., Ye *et al.*, 2013].

2.3. The Frequency Dependency of the Kinematic Rupture Process

The BP imaging also constrains the kinematics of the Okhotsk event. The rupture process was bilateral and characterized by different frequency contents in each rupture direction (Figure 2). In source images of the NA

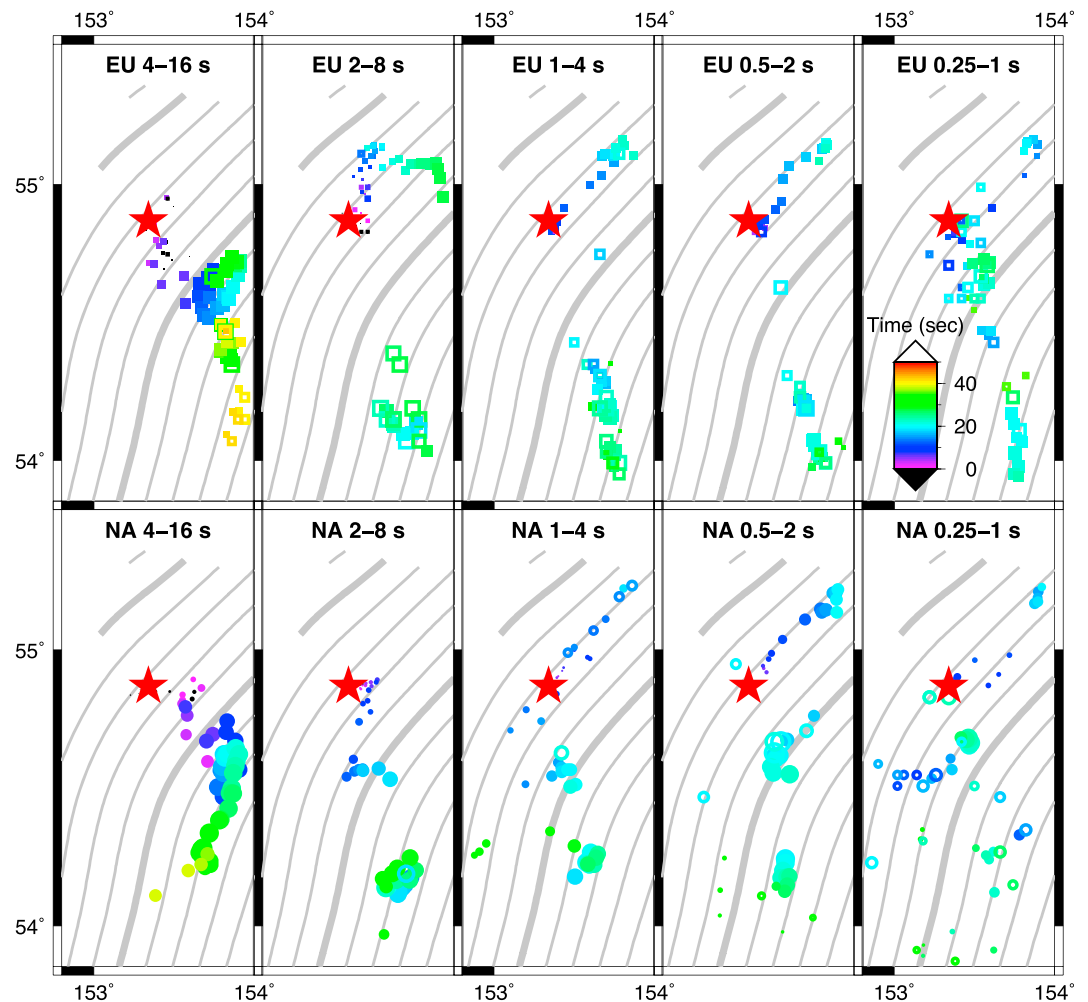


Figure 2. Spatiotemporal distribution of broadband (0.25–16 s) seismic radiation sources, imaged by the (top) European (EU) and (bottom) North America (NA) networks. The red star indicates the hypocenter location. Colored circles and squares indicate the positions of primary (filled) and significant secondary (empty) radiation sources. The significant secondary source is defined as secondary peaks whose power exceeds 50% of the primary source. Their size is scaled by beamforming amplitude, and their color indicates timing relative to hypocentral time (color scale on top right). The time increment of the BP imaging is 1 s. The gray contours denote the Slab 1.0 model with the two thick contours at depths of 600 km and 700 km.

array, the northern rupture segment extends about 50 km toward NE following the slab contours and is only visible in the high-frequency band ($f > 0.25$ Hz). The visible frequency range of the NE rupture extends down to 0.125 Hz in the EU images possibly due to the difference in azimuth and directivity. The southern rupture extends toward SSE over 90 km and is consistently observed across all frequency bands, although it appears intermittently as two individual subevents in the high-frequency imaging. In the lowest frequency band (4–16 s), a backward propagation appears in the middle of the SSE rupture (Figure 2, left), consistent with other low-frequency studies [Zhan *et al.*, 2014]. The rupture speeds in the northern and southern segments are on average about 3.4 km/s and 4.0 km/s (Figure S8), between 60% and 70% of the shear wave speed, which are compatible with the distribution of rupture speeds of other deep earthquakes [Suzuki and Yagi, 2011] and, in particular, significantly faster than the deeper 1994 Bolivian earthquake [Kanamori *et al.*, 1998].

3. Discussion and Conclusions

The broadband BP imaging provides additional high-frequency radiation constraints compared to previous studies [Zhan *et al.*, 2014], which leads to the different interpretation of a large rupture dimension beyond the

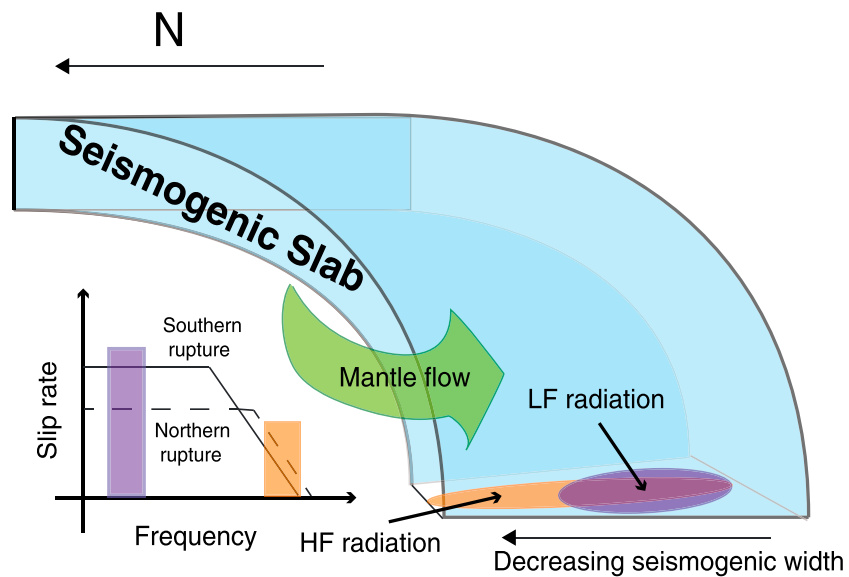


Figure 3. Schematic depiction of subducting Pacific slab (blue) with seismogenic width decreasing from south to north. The purple and orange ellipses mark the areas of low-frequency (LF) and high-frequency (HF) ruptures, respectively. The green arrow indicates the mantle flow around the edge of the slab. The bottom left inset shows an interpretative sketch of the spectra of slip rate along the northern (dashed) and southern (solid) rupture, with corner frequency inversely proportional to rise time. The northern rupture is weaker in LF radiation than the southern rupture but has stronger HF radiation possibly due to a shorter rise time controlled by a thinner seismogenic zone.

metastable olivine wedge. This implies that physical mechanisms other than, or in addition to, phase transformation are active during deep earthquake ruptures, e.g., thermal shear instability [Karato *et al.*, 2001; Kelemen and Hirth, 2007; Prieto *et al.*, 2013]. The wide aftershock distribution further suggests that the thermal shear-weakening mechanism may have created a transient weak plane that facilitates aftershock nucleation outside the metastable olivine wedge until the coseismic temperature perturbation diffuses out or that spatially heterogeneous coseismic slip left residual stresses distributed over a wide area. Both the Bolivian and Okhotsk earthquakes exhibit a wide rupture in support of the thermal shear instability mechanism. The former also features slow rupture speed, which has been associated to large-energy dissipation near the rupture front [Kanamori *et al.*, 1998; Zhan *et al.*, 2014], also known as “breakdown work” [Cocco *et al.*, 2006]. However, the significantly faster rupture speed of the Okhotsk earthquake reported here indicates that the breakdown work is not necessarily large in all earthquakes controlled by thermal runaway.

The elongated rupture pattern of the *M*7 events and the northern segment of the *M*8.2 earthquake suggest that their rupture width is limited by the thickness of the metastable olivine wedge, and hence is similar. The absence of extended off-slab rupture in the *M*7 earthquakes suggests the existence of a critical rupture length for thermal runaway, between the 40 km length of the deepest *M*7 rupture and the 60 km length of the northern *M*8.2 rupture segment. The heat induced by sliding is $H \sim \tau_d D$, where D is slip and τ_d the absolute shear stress on the fault during sliding. Static elasticity dictates $D \sim W \Delta \tau / \mu$, where W is the width of the metastable wedge, $\Delta \tau$ is the stress drop, and μ is the shear modulus. We assume that thermal instability starts when a critical heat H_c is exceeded. If $\Delta \tau$ is constant, the resulting condition for thermal runaway does not involve rupture length L . However, a larger stress drop provides larger elastic energy and favors a longer rupture, introducing a statistically correlation between $\Delta \tau$ and L . This leads to a critical rupture length for thermal runaway.

The difference in frequency content between the northern and southern rupture segments can be interpreted as a lateral variation of rise time, defined as the duration of slip at a given point of the fault. The rise time controls the frequency above which the spectrum of the slip velocity time function decays (Figure 3, inset) [Huang *et al.*, 2013]. While the southern rupture dominates the low-frequency radiation, implying larger long-period slip in the south, the northern rupture is strong in high frequency, possibly due to a shorter rise time (Figure 3, inset). We propose that this lateral variation of the rise time is controlled by the variable

thermal thickness of the slab (Figure 3). The earthquake occurred near the lateral boundary of the Pacific slab. Northeast of the hypocenter, a boundary of fast to slow velocity is visible in various tomography models [Gorbatov *et al.*, 1999; Grand, 2002; Jiang *et al.*, 2009]. This transition from cold to warm thermal state is also confirmed by a dramatic reduction of the deep seismicity rate to the north [Jiang *et al.*, 2009] (Figure S4). As the slab transits into the ambient mantle toward the north, the width between given isotherms at a given depth decreases. The slab in the north is also warmer and thinner because of the effect of the mantle flow around its edge [Levin *et al.*, 2002].

In dynamic rupture models, the rise time is ultimately limited by the width of the seismogenic zone [Day, 1982]. If temperature controls the seismogenic width of the subducting slab, this results in shorter rise time and thus more energetic high-frequency radiation in the north. An alternative interpretation is related to a finite source effect. If the whole width of the southern rupture front radiates simultaneously, it constitutes a large source compared to the high-frequency imaging wavelength, which generates a less coherent array wave field and hinders its BP imaging, allowing the northern rupture to emerge in the high frequency BP. In both interpretations, the seismogenic width controls the frequency-dependence of seismic radiation. A pure thermal control of the seismogenic width requires a rather extreme thinning of the critical isotherm along the rupture. Alternatively, the difference of seismogenic width in the north and south might be controlled by a difference of the physical mechanisms of rupture. While the SSE rupture clearly propagates beyond the metastable olivine wedge, possibly as a thermal shear instability, the NE rupture could be confined within the wedge and involve only a phase transformation instability. The thermal shear instability needs to be initiated by the phase transformation mechanism, as required by the termination of deep seismicity at the bottom of the mantle transition zone [Gleason and Green, 2009]. The *M*8.3 rupture is long enough to initiate thermal runaway in the south, but its northern transformational rupture fails to do so possibly due to the thermal thinning of the slab near its northern end. This suggests that in addition to the critical rupture length *L*, a critical width of the metastable olivine wedge is also required to trigger the thermal runaway effect. This is again supported by the elasticity argument of $D \sim W\Delta\tau/\mu$. A larger width *W* of the metastable olivine wedge leads to larger slip *D* and thus heat *H* required by the thermal runaway effect. Our observations hence suggest that while the thermal shear instability mechanism may account for a wider rupture beyond the metastable olivine wedge, the maximum rupture width is still affected by the thermal state of the subducting slab.

Acknowledgments

This research was supported by the Gordon and Betty Moore Foundation and by NSF (grant EAR-1151926). The IRIS (www.iris.edu) and the European ORFEUS (www.orfeus-eu.org) data centers provided access to broadband seismograms. The catalog of historical seismicity and aftershocks is obtained from ISC bulletin (<http://www.isc.ac.uk/>). We thank Scott French and Barbara Romanowicz for valuable discussions about tomographic models in the Kamchatka region. We thank Pei-Ru Jian and Shu-Huei Hong for discussions of the regional *M*7 deep earthquakes.

The Editor thanks two anonymous reviewers for their assistance in evaluating this paper.

References

- Antolik, M., D. Dreger, and B. Romanowicz (1996), Finite fault source study of the great 1994 deep Bolivia earthquake, *Geophys. Res. Lett.*, 23(13), 1589–1592, doi:10.1029/96GL00968.
- Chen, W. (1995), En echelon ruptures during the great Bolivian earthquake of 1994, *Geophys. Res. Lett.*, 22(16), 2261–2264, doi:10.1029/95GL01805.
- Cocco, M., P. Spudich, and E. Tinti (2006), On the mechanical work absorbed on faults during earthquake ruptures, *Geophys. Monogr. Ser.*, 170(2006), 237–254.
- Day, S. (1982), Three-dimensional finite difference simulation of fault dynamics: Rectangular faults with fixed rupture velocity, *Bull. Seismol. Soc. Am.*, 72(3), 705–727.
- Frohlich, C. (1989), The nature of deep-focus earthquakes, *Annu. Rev. Earth Planet. Sci.*, 17, 227–54.
- Gleason, G. C., and H. W. Green (2009), A general test of the hypothesis that transformation-induced faulting cannot occur in the lower mantle, *Phys. Earth Planet. Inter.*, 172(1–2), 91–103, doi:10.1016/j.pepi.2008.06.019.
- Goes, S., and J. Ritsema (1995), A broadband *P* wave analysis of the large deep Fiji Island and Bolivia earthquakes of 1994, *Geophys. Res. Lett.*, 22(16), 2249–2252, doi:10.1029/95GL02011.
- Gorbatov, A., and V. Kostoglodov (1997), Seismicity and structure of the Kamchatka subduction zone, *J. Geophys. Res.*, 102(B8), 17,883–17,898, doi:10.1029/96JB03491.
- Gorbatov, A., J. Dominguez, G. Suarez, V. Kostoglodov, D. Zhao, and E. Gordeev (1999), Tomographic imaging of the *P*-wave velocity structure beneath the Kamchatka peninsula, *Geophys. J. Int.*, 137(2), 269–279, doi:10.1046/j.1365-246X.1999.t01-1-00801.x.
- Grand, S. P. (2002), Mantle shear-wave tomography and the fate of subducted slabs, *Philos. Trans. A. Math. Phys. Eng. Sci.*, 360(1800), 2475–91, doi:10.1098/rsta.2002.1077.
- Green, H. W., and H. Houston (1995), The mechanics of deep earthquakes, *Annu. Rev. Earth Planet. Sci.*, 23(1), 169–213.
- Hayes, G. P., D. J. Wald, and R. L. Johnson (2012), Slab1.0: A three-dimensional model of global subduction zone geometries, *J. Geophys. Res.*, 117, B01302, doi:10.1029/2011JB008524.
- Huang, Y., J.-P. Ampuero, and H. Kanamori (2013), Slip-weakening models of the 2011 Tohoku-Oki earthquake and constraints on stress drop and fracture energy, *Pure Appl. Geophys.*, doi:10.1007/s00024-013-0718-2.
- Ishii, M., P. M. Shearer, H. Houston, and J. E. Vidale (2005), Extent, duration and speed of the 2004 Sumatra-Andaman earthquake imaged by the Hi-Net array, *Nature*, 435(7044), 933–936, doi:10.1038/nature03675.
- Jiang, G., D. Zhao, and G. Zhang (2009), Seismic tomography of the Pacific slab edge under Kamchatka, *Tectonophysics*, 465(1–4), 190–203, doi:10.1016/j.tecto.2008.11.019.
- Kanamori, H., D. Anderson, and T. Heaton (1998), Frictional melting during the rupture of the 1994 Bolivian earthquake, *Science*, 279(5352), 839–42.

- Karato, S., M. Riedel, and D. Yuen (2001), Rheological structure and deformation of subducted slabs in the mantle transition zone: Implications for mantle circulation and deep earthquakes, *Phys. Earth Planet. Inter.*, 127(1–4), 83–108, doi:10.1016/S0031-9201(01)00223-0.
- Kelemen, P. B., and G. Hirth (2007), A periodic shear-heating mechanism for intermediate-depth earthquakes in the mantle, *Nature*, 446(7137), 787–90, doi:10.1038/nature05717.
- Kikuchi, M., and H. Kanamori (1994), The deep Bolivia earthquake of June 9, 1994, *Geophys. Res. Lett.*, 21(22), 2341–2344, doi:10.1029/94GL02483.
- Kirby, S., S. Stein, E. Okal, and D. Rubie (1996), Metastable mantle phase transformations and deep earthquakes in subducting oceanic lithosphere, *Rev. Geophys.*, 34(2), 261–306, doi:10.1029/96RG01050.
- Kiser, E., M. Ishii, C. H. Langmuir, P. M. Shearer, and H. Hirose (2011), Insights into the mechanism of intermediate-depth earthquakes from source properties as imaged by back projection of multiple seismic phases, *J. Geophys. Res.*, 116, B06310, doi:10.1029/2010JB007831.
- Koper, K. D., A. R. Hutko, T. Lay, and O. Sufri (2012), Imaging short-period seismic radiation from the 27 February 2010 Chile (MW 8.8) earthquake by back-projection of P, PP, and PKIKP waves, *J. Geophys. Res.*, 117, B02308, doi:10.1029/2011JB008576.
- Levin, V., N. Shapiro, J. Park, and M. Ritzwoller (2002), Seismic evidence for catastrophic slab loss beneath Kamchatka, *Nature*, 418(August), 763–767, doi:10.1038/nature00979.1.
- Marone, C., and M. Liu (1997), Transformation shear instability and the seismogenic zone for deep earthquakes, *Geophys. Res. Lett.*, 24(15), 1887–1890, doi:10.1029/97GL01851.
- Meng, L., A. Inbal, and J.-P. Ampuero (2011), A window into the complexity of the dynamic rupture of the 2011 Mw 9 Tohoku-Oki earthquake, *Geophys. Res. Lett.*, 38, L00G07, doi:10.1029/2011GL048118.
- Meng, L., J. Ampuero, Y. Luo, W. Wu, and S. Ni (2013), Mitigating artifacts in back-projection source imaging with implications for frequency-dependent properties of the Tohoku-Oki earthquake, *Earth Planet. Space*, 64(12), 1101–1109, doi:10.5047/eps.2012.05.010.
- Prieto, G. A., M. Florez, S. A. Barrett, G. C. Beroza, P. Pedraza, J. F. Blanco, and E. Poveda (2013), Seismic evidence for thermal runaway during intermediate-depth earthquake rupture, *Geophys. Res. Lett.*, 40, 6064–6068, doi:10.1002/2013GL058109.
- Silver, P., and S. Beck (1995), Rupture characteristics of the deep Bolivian earthquake of 9 June 1994 and the mechanism of deep-focus earthquakes, *Science*, 268(5207), 69–73.
- Suzuki, M., and Y. Yagi (2011), Depth dependence of rupture velocity in deep earthquakes, *Geophys. Res. Lett.*, 38, L05308, doi:10.1029/2011GL046807.
- Tibi, R., C. Estabrook, and G. Bock (1999), The 1996 June 17 Flores Sea and 1994 March 9 Fiji—Tonga earthquakes: Source processes and deep earthquake mechanisms, *Geophys. J. Int.*, 138, 625–642.
- Warren, L. M., M. A. Langstaff, and P. G. Silver (2008), Fault plane orientations of intermediate-depth earthquakes in the Middle America Trench, *J. Geophys. Res.*, 113, B01304, doi:10.1029/2007JB005028.
- Ye, L., T. Lay, H. Kanamori, and K. D. Koper (2013), Energy release of the 2013 Mw 8.3 Sea of Okhotsk earthquake and deep slab stress heterogeneity, *Science*, 341(6152), 1380–1384, doi:10.1126/science.1242032.
- Zhan, Z., H. Kanamori, V. C. Tsai, D. V. Helmberger, and S. Wei (2014), Rupture complexity of the 1994 Bolivia and 2013 Sea of Okhotsk deep earthquakes, *Earth Planet. Sci. Lett.*, 385, 89–96, doi:10.1016/j.epsl.2013.10.028.